

International Journal of Modern Physics C
 © World Scientific Publishing Company

Improved phase-field-based lattice Boltzmann models with a filtered collision operator

Hiroshi Otomo, Raoyang Zhang, Hudong Chen

Dassault Systèmes, 55 Network Drive, Burlington, MA 01803, USA
Hiroshi.Otomo@3ds.com

Received Day Month Year
 Revised Day Month Year

In this study, a phase-field lattice Boltzmann model based on the Allen-Cahn equation with a filtered collision operator and high-order corrections in the equilibrium distribution functions is presented. Here we show that in addition to producing numerical results consistent with prior numerical methods, analytic solutions, and experiments with the density ratio of 1000, previous numerical deficiencies are resolved. Specifically, the new model is characterized by robustness at low viscosity, accurate prediction of shear stress at interfaces, and removal of artificial dense bubbles and rarefied droplets, etc.

Keywords: phase-field lattice Boltzmann model; Allen-Cahn equation; filtered collision operator; high density ratio

PACS Nos.: 11.25.Hf, 123.1K

1. Introduction

The modified Allen-Cahn (AC) equation, in which curvature driven dynamics is eliminated^{1,2}, is widely studied as an efficient interface-tracking solver in multiphase flow with high density ratio due to its robustness and handiness of the conserved second-order partial differential equation.

In previous studies^{3,4}, a second set of the distribution functions is introduced to solve the AC equation for the interface dynamics, which is coupled with the hydrodynamic lattice Boltzmann (LB) based momentum solver. In order to improve stability at low viscosity and accuracy around interfaces, the multiple relaxation time (MRT) scheme and the biased difference scheme for the gradient of the order parameter were implemented³. The MRT scheme, however, suffers from high computational costs and a large number of model parameters. Also, due to using the biased difference scheme, the requirement of information from sites next to the nearest neighbors causes difficulties in near boundary regions, which may involve nontrivial extrapolation, complex code vectorization and parallelization, and additional computational cost.

In the present study, our LB model is formulated with a filtered collision operator^{5,6,7,8,9,10} with a single relaxation time. The central difference scheme,

which only requires information at nearest neighbor sites, is applied because of its high computational efficiency. It is known that the truncation error of the central difference scheme may cause inaccurate shear stress on interfaces¹³. Also, the original AC equation may inevitably produce artificial dense bubbles and rarefied droplets. We propose a single solution to both of these unphysical effects and present numerical results from our improved model where these undesirable features are mitigated. All validation cases are conducted with a single source code containing our newly proposed algorithm.

2. Lattice Boltzmann models

Two lattice Boltzmann (LB) equations, one for the order parameter ϕ and the other for hydrodynamic quantities such as pressure P and momentum $\rho\vec{u}$ are solved. For both equations, the D3Q19 or D2Q9 lattice model is adopted with index $i \in \{1, \dots, 19\}$ or $i \in \{1, \dots, 9\}$.

Formulation of the LB equation for ϕ follows the previous study³,

$$h_i(\vec{x} + \vec{c}_i\Delta t, t + \Delta t) = h_i(\vec{x}, t) - \frac{h_i - h_i^{eq}}{(M/T) + 0.5}|_{\vec{x}, t}, \quad (1)$$

where M is the mobility and h_i^{eq} is the equilibrium state defined as,

$$h_i^{eq} = \phi\Gamma_i + \theta w_i(\vec{c}_i \cdot \vec{n}), \quad (2)$$

$$\Gamma_i = w_i \left\{ 1 + \frac{\vec{c}_i \cdot \vec{u}}{T} + \frac{(\vec{c}_i \cdot \vec{u})^2}{2T^2} - \frac{\vec{u}^2}{2T} \right\}, \quad (3)$$

$$\theta = \frac{M}{T} \left\{ \frac{1 - 4(\phi - 0.5)^2}{W} \right\}. \quad (4)$$

Here W is the interface thickness and \vec{n} is the unit vector normal to the interface calculated by $\vec{\nabla}\phi / (|\vec{\nabla}\phi| + \epsilon)$ where ϵ is a tiny parameter such as $1.e - 10$ in order to avoid division by zero. The value of ϕ is evaluated by $\sum_i h_i$.

Formulation of the hydrodynamic LB equation is based on the previous study³. One with the BGK collision operator is,

$$\bar{g}_i(\vec{x} + \vec{c}_i\Delta t, t + \Delta t) = \bar{g}_i(\vec{x}, t) - \frac{\bar{g}_i - \bar{g}_i^{eq}}{\tau_{mix}}|_{\vec{x}, t} + K_i(\vec{x}, t), \quad (5)$$

where

$$\bar{g}_i^{eq} = \rho\Gamma_i + w_i \left(\frac{P}{T} - \rho \right) - \frac{K_i}{2}, \quad (6)$$

$$K_i = \left\{ (\Gamma_i - w_i) \rho_{dif} + \frac{\Gamma_i \mu_{chm}}{T} \right\} (\vec{c}_i - \vec{u}) \cdot \vec{\nabla}\phi + \Gamma_i \frac{(\vec{c}_i - \vec{u}) \cdot \vec{F}_{ex}}{T}. \quad (7)$$

Here K_i is a force term responsible for phase separation and the external force \vec{F}_{ex} . ρ_{dif} is difference between the light and heavy characteristic density ρ . μ_{chm} is the

chemical potential defined as,

$$\mu_{chm} = \frac{48\sigma}{W}\phi(\phi - 1)(\phi - 0.5) - \frac{3\sigma W}{2}\vec{\nabla}^2\phi, \quad (8)$$

where σ is the surface tension.

The relaxation time τ_{mix} is approximated using the harmonic interpolation,

$$1/\tau_{mix} = (1/\tau_{air}) + \phi \{ (1/\tau_{water}) - (1/\tau_{air}) \}, \quad (9)$$

with relaxation times of water and air, τ_{water} and τ_{air} , which correspond to their kinematic viscosities, ν_{water} and ν_{air} .

The right hand side in Eq. (5) is filtered as,

$$\bar{g}_i(\vec{x} + \vec{c}_i\Delta t, t + \Delta t) = \bar{G}_i^{eq} + \left(1 - \frac{1}{\tau_{mix}}\right) \Phi_i : \Pi, \quad (10)$$

where Φ_i is a filtered operator that uses Hermite polynomials and Π is the nonequilibrium moments of the momentum flux,

$$\Phi_i = \frac{w_i}{2T^2} (\vec{c}_i\vec{c}_i - TI), \quad (11)$$

$$\Pi = \sum_l \vec{c}_l\vec{c}_l (\bar{g}_l - \bar{G}_l^{neq}). \quad (12)$$

Here I is the identity matrix. The equilibrium and nonequilibrium parts \bar{G}_i^{eq} and \bar{G}_i^{neq} are naturally determined via correspondence with Eq. (5) and τ_{mix} dependence. More details of filtered collision procedure can be found in previous studies 5,6,7,8,9,10,11,12. Projection from the state-space to moment-space is performed in Eq. (12) only for 9 moments in the case of D3Q19. Also, since the spatially dependent relaxation time τ_{mix} is factored out from the projected term in Eq. (10), the calculation of $\Phi_i : \Pi$ can be simplified down to the multiplication between a 19×19 matrix^a and a 1×19 matrix. On the other hand, in the MRT scheme the projection is performed for the 19 moments on D3Q19 via the multiplication of the matrix $M^{-1}DM$ where M is the 19×19 conversion matrix from the state-space to the moment space and D is the 19th-rank diagonal matrix involving the relaxation time. This multiplication of matrices is known to cause deterioration of computational efficiency. As a result, the filtering discussed in the present study can possess much higher computational efficiency compared to the MRT scheme.

After Eq. (10) is solved, pressure and momentum are evaluated by $T \sum_i \bar{g}_i + (T\rho_{dif}/2) \vec{u} \cdot \vec{\nabla} \phi$ and $\sum_i \vec{c}_i \bar{g}_i + (\mu_{chm} \vec{\nabla} \phi + \vec{F}_{ex})/2$, respectively.

In this study, the gradient and Laplacian of ϕ , that are used for calculation of \vec{n} , P , $\rho\vec{u}$, and K_i , are approximated with the central difference (CD) scheme,

$$\vec{\nabla} \phi = \frac{\sum_i \{ \phi(\vec{x} + \vec{c}_i) - \phi(\vec{x} - \vec{c}_i) \} \vec{c}_i w_i}{2T}, \quad \vec{\nabla}^2 \phi = \frac{2 \sum_i \{ \phi(\vec{x} + \vec{c}_i) - \phi(\vec{x}) \} w_i}{T}.$$

^aSimply following Eq. (11) and Eq. (12), we can decompose this 19×19 matrix to the multiplication between a 19×3 matrix and a 3×19 matrix so that the operation count is saved further.

This discretization scheme requires information only from the nearest neighbor sites, whereas existing implementations utilizing biased differencing use next-nearest neighbor sites. For all results shown in this manuscript, unless specifically mentioned, the density ratio $\rho_{ratio} = \rho_{water}/\rho_{air}$ is 1000, consistent with air - water mixtures. The dynamic viscosity ratio μ_{water}/μ_{air} is denoted as μ_{ratio} .

3. Pathological cases

In spite of high computational efficiency, the LB models described in the previous section are inadequate for some benchmark cases. In this section, a few simple cases are chosen as pathological cases and the remedies are proposed.

First, with the LB models in Section 2, shear stress on the interface is not evaluated accurately. In Fig. 1, numerical results for two-phase Poiseuille flow and Couette flow are shown. In both cases, water occupied the left half domain and air is on the right half side. The domain sizes L are 64 and 100 for each case. $\mu_{ratio} = 100$, $\nu_{water} = 0.17$, $M = 0.1$, and $W = 2.5$ for both cases. Gravitational acceleration $g = 1.0e - 6$ is applied in the Poiseuille flow. The analytic solutions are derived while density profiles with non-zero interface thickness and viscosity in the mixture are taken into account.

Results of the LB models in Section 2 show peaks on the interface and deviate from analytic solutions obviously. Since the similar behavior is observed even with the MRT collision operator in the previous study¹⁴ if they use the pure CD scheme, it is not mainly due to the filtered collision operator but likely due to the CD scheme. Indeed, our analysis reveals that irregular effects at the interface originated from some high-order terms such as $\partial_x (v_y \partial_x^3 \rho)$ in the Navier-Stokes (NS) equation where the CD scheme is used. Although using the biased scheme can solve the issue as the study¹³ indicated, such an approach requires information from sites farther than the nearest neighbors, resulting in computational complexities. Instead, a high order correction in the equilibrium distribution is added as the following in the present work together with the CD scheme and modification of definition of velocity so that the term $\partial_x (v_y \partial_x^3 \rho)$ is removed,

$$\delta f_i^{eq} = \frac{1}{4T} w_i (\vec{c}_i \cdot \vec{u}) \vec{\nabla}^2 \rho. \quad (13)$$

Fig. 1 shows results of the modified model marked as ‘‘Present’’ matching with analytic solutions very well.

It is worth mentioning that this issue may be sometimes hidden in pressure or force driven flow⁴ because the higher density side has relatively lower velocity. Due to the same reason, if velocity is assigned on a wall of the air side in the Couette flow, the velocity with the original models apparently matches with the analytic solution as shown in the right figure of Fig. 1.

Here we would like to emphasize that the purpose of comparisons in Fig. 1 is to check the local balance of shear stress in each lattice by taking account of the

non-zero interface thickness and fixing the interpolation of viscosity on the interface. This is different from a recent paper¹³, in which the interpolation method of τ_{mix} is studied. In our study, if the formula in Eq. (9) is changed, both of analytic solutions and numerical results are changed in Fig. 1.

In the previous study¹³, this issue was improved with the so-called velocity-based LB model, in which the first moment of the distribution function is velocity instead of momentum. Therefore, in contrast to the momentum-based LB model used in the present work, density and velocity are conserved independently, but there is no guarantee of momentum conservation during the particle advection even at zero surface tension.

Furthermore, this modified LB model also improves the Galilean invariance. In the one-dimensional domain of $L=100$ bounded by periodic boundaries, the droplet is sitting in the center and a value of 0.025 for lattice velocity is homogeneously assigned initially. $\nu_{water} = 1.7e - 2$ and $W = 3.0$. The rest of settings are the same as in the above cases of Couette flow. In Fig. 2, profiles of ϕ and velocity v_x are presented in terms of the cycle period during which the droplet comes back to the original position. As seen here, though droplets' movements are similar with both models, the velocity with the modified model maintains a constant value and preserves Galilean invariance during the entire evolution, while the velocity with the original model described in Section 2 fails.

Second, with the LB models for ϕ from Section 2, a large number of unphysical droplets/bubbles whose ϕ is close to 0/1, can be produced. In order to clarify this issue, a simple two-dimensional case is set as shown in the left figure of Fig. 3. Here, the lattice velocity of 0.05 is assigned in the thin layer of water domain. $\mu_{ratio} = 1$, $\nu_{water} = 1.7e - 1$, $W = 3.0$, and $M = 1.7e - 1$. The shock created by initial velocity is reflected on the top and bottom edges of domain and bounces back and forth for a while. It produces a lot of bubbles which stay in the water domain even after the steady state is reached as shown in the center figure of Fig. 3. Because of the steady state, it is likely that the value of the mobility does not depend on the solution of these bubbles in the AC equation. As the contour's range indicates, these are dense bubbles, whose ϕ is 0.90 – 0.99. They are totally different from the "decent" bubbles, whose ϕ goes down to zero in their centers. Hence such dense bubbles are insensitive to buoyancy force and sometimes distort streamlines. This issue seems to be originated from the Allen-Cahn model, that prompts the nucleation of droplets and bubbles no matter how much ϕ they have. In order to solve this problem, a minor diffusion correction is added to the Allen-Cahn model via θ in Eq. (4) so that such bubbles are diffused. Specifically, θ is corrected as,

$$\delta\theta = C \frac{M}{T} F(\phi, \vec{\nabla}^2 \phi) |\vec{\nabla} \phi|, \quad (14)$$

where C is a constant value. There are various choices of function F but it is

determined so that this correction is turned off for the decent bubbles and droplets. As a result, dense bubbles disappear as seen in the right figure of Fig. 3. In the test cases discussed in the next section, no obvious issues resulting from this modification are observed. It indicates that the main interface dynamics is insensitive to this minor diffusion correction. The similar problem of rarefied droplets in the air domain can be improved with a similar modification.

4. A set of regular validation cases

4.1. A static droplet

Through the simulation of a static droplet in free space, consistence with the Laplace law is examined and the spurious current is compared to the other multi-phase LB models. A two-dimensional static droplet with variable initial radius, $R = \{8, 12, 16\}$, is put in the center of domain, whose size is five times of R and periodic boundaries are assigned on each pair of domain's edges. $\nu_{water} = \{3.3e-4, 1.7e-1\}$, $\mu_{ratio} = 60$, $M = 0.1$, and $W = 2.5$. First, with a small viscosity of $\nu_{water} = 3.3e-4$, a droplet with $\sigma = \{1.0e-2, 6.0e-3, 1.0e-3\}$ is simulated. The left figure of Fig. 4 shows the relation between $1/R$ and the pressure difference across the interface, dP . Lines with slopes of inputted σ are presented. All cases comply with the Laplace law, $dP = \sigma/R$, very well and output the consistent value of σ . Next, spatially-averaged spurious current of a droplet of $R=40$ is measured for various σ in the periodic domain of 250×250 . In the right figure of Fig. 4, results with $\nu_{water} = \{1.7e-1, 3.3e-4\}$ are compared to the previous study¹⁵ in which the recent pseudo-potential model for $\rho_{ratio} = 1000$ is used. While more diffusion with higher viscosity leads to less spurious current, the difference between two viscosity options becomes small as σ is increased. The phase-field LB model in this study shows much improved spurious current than the recent pseudo-potential model by factor of $10^3 - 10^4$ for this droplet case of $\rho_{ratio} = 1000$.

4.2. Droplet collision

Binary droplet collisions are often simulated in order to check the interface dynamics and robustness of computational models for multi-phase flows with high-density ratio^{15,16,17}. In this study, a binary droplet collision under two flow conditions are compared to experimental results¹⁸. For each case, the droplet diameter is $\{32, 50\}$, $\sigma = \{5.5, 0.64\}$, and $\nu_{water} = \{1.9e-3, 6.0e-4\}$. $\nu_{ratio} = 60$, $M = 0.1$ and $W = 2.5$. The relative velocity U is set as 0.1 and 0.75 for the case with coarse and fine resolution, respectively. Hence Reynold number Re , UD/ν_{water} , is $\{1700, 6300\}$ and Weber number We , $\rho_{water}U^2D/\sigma$, is $\{58, 440\}$, respectively. As shown in Fig. 5, the simulated droplets' deformation and splashing patterns depending on Re and We seem to be comparable with Fig. 2 and Fig. 4(a) in the paper¹⁸. Compared to a previous study with the recent pseudo-potential LB model for $\rho_{ratio} = 1000$ ¹⁵, similar accuracy can be achieved using half interface thickness and quarter resolution approximately in this study.

4.3. Rayleigh-Taylor instability

Rayleigh-Taylor instability induced by heavy fluid's penetration into light fluid with gravity is simulated as a benchmark problem for the interface dynamics. Numerical results are compared to previous studies^{13,19}. Two cases using $\rho_{ratio} = \{3, 1000\}$ are tested in two-dimensional domains of $\{150 \times 600, 256 \times 1000\}$, whose horizontal lengths are denoted as L . For each case, $\sigma = \{8.6e - 4, 4.7e - 1\}$, $\mu_{ratio} = \{1, 100\}$, $W = \{2.5, 5.0\}$, $M = \{5.8e - 3, 1.3e - 2\}$, and $\nu_{water} = \{1.9e - 3, 4.1e - 3\}$, respectively. Gravitational acceleration g is set as $1.e - 5$ for both cases. Accordingly, if the characteristic velocity U is estimated as \sqrt{gL} , $Re = UL/\nu_{water} = 3000$ and the Péclet number, UL/M , is 1000 approximately. Capillary number, $\rho_{water}U\nu_{water}/\sigma$, is $\{0.26, 0.44\}$, respectively. In the left and center figures of Fig. 6 contours of ϕ and histories of bubble/liquid front normalized by L where $\rho_{ratio} = 3$ are presented. The non-dimensional time t^* is defined as $t\sqrt{g/L}$. The penetration pattern and its quantitative positions are consistent with previous studies¹⁹, in which a finite element method was used. In the right figure of Fig. 6, contours of ϕ with $\rho_{ratio} = 1000$ are shown. Compared to results of the previous study¹³ with the velocity-based phase-field LB models, the same-level robust results are captured while W seems to be smaller and the finger shape is slightly sharper in the present study.

4.4. Dam-breaking case

In a recent study²⁰, dynamics of the dam-breaking wave is investigated experimentally by measuring the water heights and the impact pressure on the downstream vertical wall. This case is simulated with the LB models in this study and measurements are compared with the experiment.

The computational domain of $537 \times 198 \times 50$ is bounded by friction walls except for the top boundary of the pressure condition. The initial height of water column H is 100. $g = 4.0e - 6$. $W = 4.0$, $M = 0.02$, and $\nu_{air} = 8.3e - 3$. $\sigma = 5.2e - 3$ and $\nu_{water} = 4.9e - 6$ so that the Weber number is $7.7e3$ and the Reynolds number of water is $4.1e5$. The sensors' positions for the pressure measurement are shown in Fig. 7. The water heights are detected on three lines, D1 through D3, located in the center of the z -coordinate.

In Fig. 7, the measured pressure, the surge-front position of water, and water heights are compared with the experimental results. Results for pressure, front position, and water height are nearly consistent with observations. We note that although our proposed model lacks treatment for turbulence and the simulations are underresolved for the Reynolds number used, the physical structures captured by our model are nearly consistent with experiments. In the beginning stage, the surge-front position is slightly underestimated due to the initial condition. We believe the prediction of the pressure peak may be improved with increased spatial resolution.

5. Summary

An improved phase-field lattice Boltzmann model based on the Allen-Cahn equation with the filtered collision operator and the equilibrium distribution with a high-order correction in the LB equations for ϕ and hydrodynamic quantities is introduced without sacrificing the simplicity of algorithm and computational cost significantly. These modifications improve solver robustness at low viscosity, accuracy of shear stress at interfaces, the Galilean invariance, and production of artificial dense bubbles and rarefied droplets. In addition to extremely low spurious current, the same accuracy as the recent pseudo-potential model is achieved using half of the interface thickness and a quarter of resolution. Across various cases, consistent results with other numerical methods, analytic solutions and experiments are obtained with the efficient choices of parameters such as the resolution and the interface thickness.

Acknowledgments

H.O. would like to thank Takaji Inamuro and Taehun Lee for effective and enlightening discussions. We would also like to thank Luca D'Alessio for discussing setups of test cases. Also, we express gratitude to Casey Bartlett and Ilya Staroselsky for valuable comments on this study.

References

1. Y.Sun and C.Beckermann, *J Comput. Phys.* **220**, 626-653 (2007).
2. P.H.Chiu and Y.T.Lin, *J Comput. Phys.* **230**, 185-204 (2011).
3. A.Fakhari, M.Geier and T.Lee, *J. Comput. Phys.* **315**, 434-457 (2016).
4. H.Liang, J.Xu, J.Chen, H.Wang, Z.Chai and B.Shi, *Phys. Rev. E* **97**, 033309 (2017).
5. H.Chen, R.Zhang, I.Staroselsky and M.Jhon, *Physica A* **362**, 125 (2006).
6. R.Zhang, X.Shan and H.Chen, *Phys. Rev. E* **74**, 046703 (2006).
7. J.Latt and B.Chopard, *Math. Comput. Simulat.* **72**, 2-6 (2006).
8. X.Shan, X.F.Yuan and H.Chen, *J. Fluid Mech.* **550**, 413 (2006).
9. H.Chen, R. Zhang and P. Gopalakrishnan, *US Patent 9576087* (2013).
10. H.Chen, P. Gopalakrishnan and R. Zhang, *Int. J. Mod. Phys. C* **25**, 1450046 (2014).
11. H.Otomo, H. Fan, Y. Li, M. Dressler, I. Staroselsky, R.Zhang, and H.Chen, *J. Comput. Sci.* **17**, 334 (2016).
12. H. Otomo, B. Crouse, M. Dressler, D.M. Freed, I. Staroselsky, R.Zhang, and H.Chen, *Comput. Fluids.* **172**, 674-682 (2018).
13. A.Fakhari, T.Mitchell, C.Leonardi and D.Bolster, *Phys. Rev. E* **96**, 053301 (2017).
14. A.Fakhari and D.Bolster, *J Comput. Phys.* **334**, 620 (2017).
15. D.Lycett-Brown and K.H.Luo, *Phys. Rev. E* **94**, 053313 (2016).
16. T.Inamuro, T.Ogata, S.Tajima and N.Konishi, *J Comput. Phys.* **198**, 628 (2004).
17. T.Inamuro, T.Yokoyama, K.Tanaka and M.Taniguchi, *Comput. Fluids.* **137**, 55-69 (2016).
18. K.H. Pan, P.C.Chou and Y.J.Tseng, *Phys. Rev. E* **80**, 036301 (2009).
19. J.L.Guermond and L.Quartapelle, *J. Comput. Phys.* **165**, 167-188 (2000).
20. L.Lobovsky, E.Botia-Vera, F.Castellana, J.Mas-Soler, A.Souto-Iglesias, *J. Fluids. Struct.* **48**, 407-434 (2014).

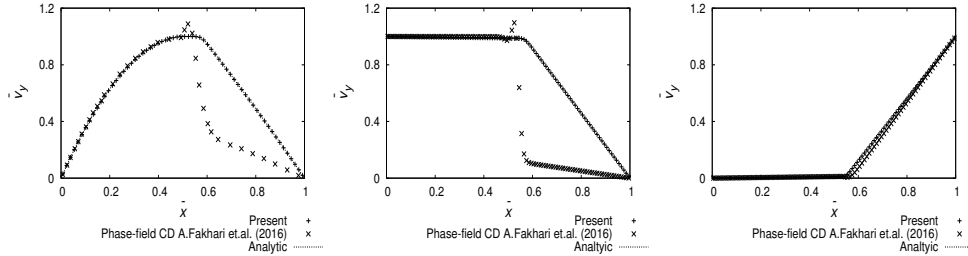


Fig. 1. Velocity profile of multi-phase Poiseuille (left) and Couette (center and right) flow normalized by maximum velocity in the analytic solution. The x-axis is normalized coordinates by the domain size L . Results with our modified LB model are plotted as 'Present' accompanied with analytic solutions and results with the LB models in Section 2 with the central difference scheme. In the Couette flow, velocity is assigned on the left wall (center) and right wall (right), respectively.

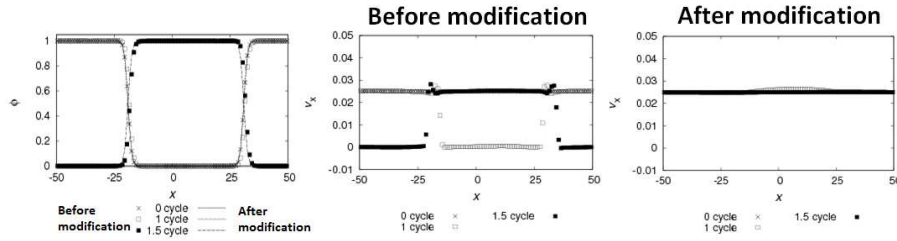


Fig. 2. Profiles of ϕ (left) and velocity v_x with the original LB models (center) and the modified LB models (right) in terms of cyclic periods of droplet's movement.

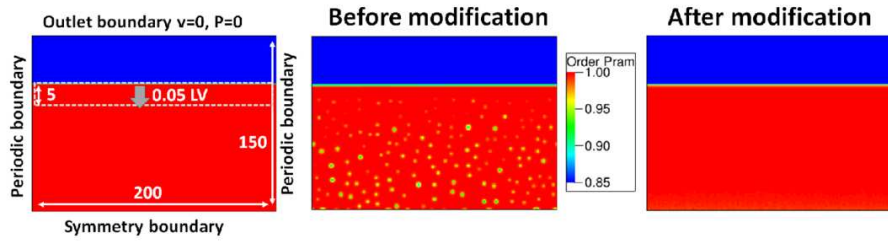


Fig. 3. Settings of an initial shock case (left). Its numerical results of ϕ ranging 0.85-1.0 at steady states with the original (center) and modified (right) LB models. The central difference scheme is used for calculations of \bar{n} , P , $\rho\bar{u}$, and K_i . $M = 1.7e - 1$.

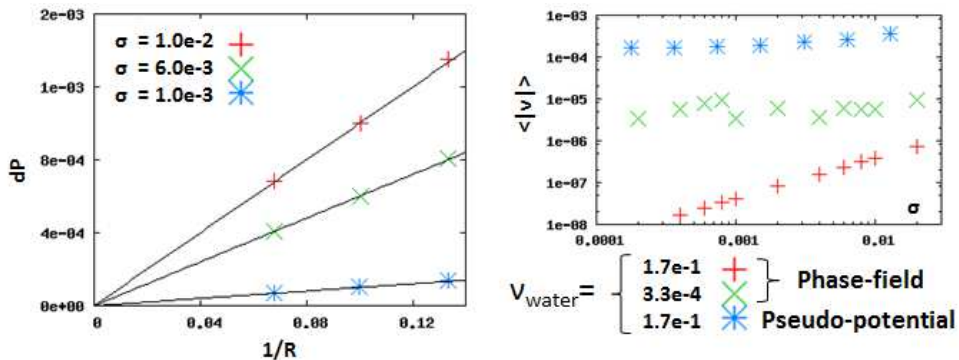


Fig. 4. Inverse droplet radius $1/R$ vs pressure difference dP across the droplet interface (left). Surface tension σ vs spatial averaged spurious current $\langle |v| \rangle$ with $v_{water} = \{3.3e - 4, 1.7e - 1\}$ (right). Results are compared to a recent study of the pseudo-potential model for $\rho_{ratio} = 1000$.

10

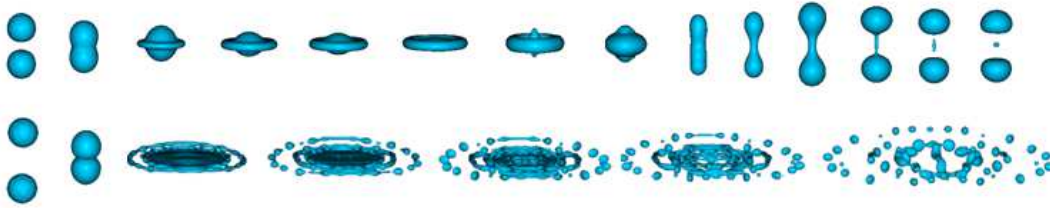


Fig. 5. Snapshots of a binary droplet collision. Reynolds numbers are 1700 (top) and 6300 (bottom). Weber numbers are 58 (top) and 440 (bottom).

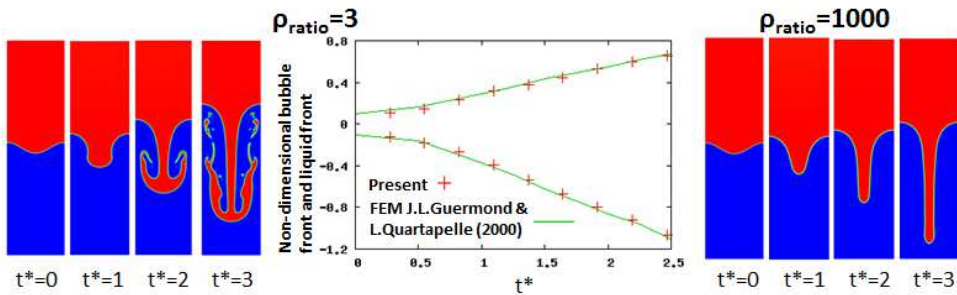


Fig. 6. Contours of ϕ where $\rho_{ratio} = 3$ (left) and 1000 (right), and histories of bubble/liquid front normalized by L where $\rho_{ratio} = 3$ (center) in Rayleigh Taylor instability. In the center figure, results of a previous study with the finite element method (FEM) are compared. $t^* = t\sqrt{g/L}$.

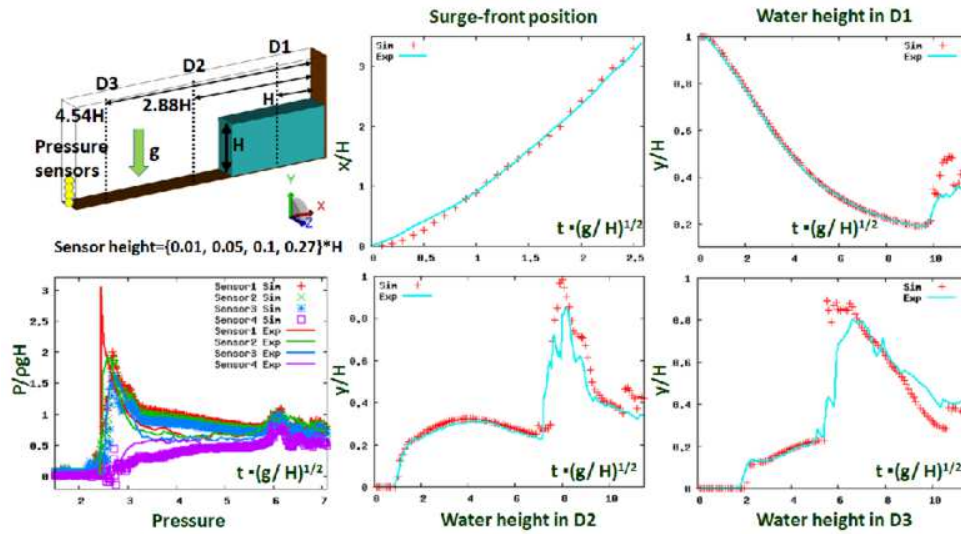


Fig. 7. In the dam-breaking case, settings (left top), comparisons of the surge-front position (center top), pressure on the wall (left bottom), and water heights (others) between the simulation displayed as 'Sim' and the experiment displayed as 'Exp'